Numerical study of liquid metal magnetoconvection and heat transfer in an electrically conductive square duct

Fico, Francesco; Xia, Hao; Langella, Ivan; Politis, Gerasimos

DOI
10.1016/j.ijheatmasstransfer.2024.125857

Publication date
2024

Document Version
Final published version

Published in
International Journal of Heat and Mass Transfer

International Journal of Heat and Mass Transfer 231 (2024) 125857

Contents lists available at ScienceDirect

International Journal of Heat and Mass Transfer

journal homepage: www.elsevier.com/locate/hmt

Numerical study of liquid metal magnetoconvection and heat transfer in an electrically conductive square duct

Francesco Fico [a,*], Hao Xia [a], Ivan Langella [b], Gerasimos Politis [c]

[a] Aeronautical and Automotive Engineering, Loughborough University, Loughborough, United Kingdom
[b] Aerospace Engineering, Flight Performance and Propulsion, TU Delft, Delft, Netherlands
[c] UK Atomic Energy Authority, Abingdon, United Kingdom

ARTICLE INFO

Keywords:
MHD
Mixed convection
Turbulence
LES

ABSTRACT

Mixed convection of an electrically conductive fluid in a square duct with imposed transverse magnetic field is studied using Large Eddy Simulation (LES) paradigms. The duct walls are electrically conductive, with the wall conductivity parameter c_w ranging from 0 to 0.5. The Reynolds number is Re = 5602 and the Prandtl number is Pr = 0.0238. The focus of the study is on flows at Hartmann numbers Ha $\leqslant$ 125, Richardson numbers Ri $\leqslant$ 10 and two different thermal boundary conditions are considered: four wall uniform heat fluxes and one-sided heating (fixed wall temperature). The results show that the transition from laminar to turbulent flow depends not only on the ratio Ri/Ha, but also on c_w and on the local thermal boundary conditions. In the turbulent regime with one-sided heating, the turbulent heat fluxes play an important role in the total heat transfer, in contrast with the typical behaviours of liquid metals. Moreover, the turbulent and thermal structures are highly dependent on the thermal boundary conditions, which completely alter the flow structure. It is also found that at $c_w \geq 0.01$ the turbulent heat fluxes decrease.

1. Introduction

The study of liquid metals mixed convection within magnetic fields plays an essential role in many engineering applications: metallurgy, geothermal energy extraction, and in particular fusion reactors [1]. In the latter, interest in heat and mass transfer in liquid metals under strong magnetic fields is largely stimulated by their application as a coolant and working fluid [2]. In this context, lithium-containing metal compounds are promising candidates due to their use as tritium breeders [3]. Several competing concepts of blanket modules are currently being pursued: self-cooled blanket [4,5], dual-cooled lithium-lead (DCLL) blanket [6,7], helium-cooled lead lithium(HCLL) blanket [8,9] and water-cooled lead lithium (WCLL) [10,11]. The mentioned configurations, each with slightly different optimization objective, generally endeavour to breed tritium, extract the heat from the nuclear reaction and shield components from radiation exposure, while minimizing the magnetohydrodynamics (MHD) induced pressure drop.

The nature of liquid metal flows is unique and very different from the nature of the flows commonly studied in the context of heat transfer problems. One reason is the very low Prandtl number of liquid metals for which heat transfer significantly differs from that of conventional coolants. At the typical Prandtl number of liquid metals, the smallest temperature scales are much larger than the corresponding velocity scales, indicating that heat transfer tends to be mostly conductive [12]. On the other hand, the magnetic field deeply affects the liquid metal flow, flattening the velocity profile and suppressing the turbulent fluctuations [13,14], with non-convectional quasi two-dimensional (Q2D) turbulence states also appearing [15]. The peculiarity of the liquid metal flows in such systems is the combination of large flow rate, high temperature gradients and strong magnetic field. The dimensionless parameters which characterize the flow rate, the magnetic field, and the heating, are Reynolds ($\mathrm{Re} = U_b D_h/\nu$), Hartmann ($\mathrm{Ha} = B_0 D_h \sqrt{\sigma/\mu}$) and Grashof ($\mathrm{Gr} = g\beta\Delta T D_h^3 \nu^{-2}$ or $\mathrm{Gr} = g\beta q_w D_h^4 \nu^{-2}\lambda^{-1}$) numbers, where $U_b, D_h, \nu, B_0, \sigma, \mu, g, \Delta T, \beta, q_w$ and λ are the bulk velocity, characteristic length, kinematic viscosity, magnetic field, electrical conductivity, dynamic viscosity, gravity, gap temperature, thermal expansion coefficient, heat flux and thermal conductivity respectively. Additionally, the Richardson number Ri (defining the ratio between the buoyancy and inertial forces), the Stuart number N (defining the ratio between the Lorentz and inertial forces), and the Reynolds Hartmann number ratio Rh, defined respectively as:

$$\mathrm{Ri} = \frac{Gr}{\mathrm{Re}^2}, \quad N = \frac{\mathrm{Ha}^2}{\mathrm{Re}}, \quad Rh = \frac{\mathrm{Re}}{\mathrm{Ha}} = \frac{u\delta_h}{\nu} \tag{1}$$

provide a measure of the relation between the various forces, where u, ν and δ_h are the velocity, kinematic viscosity and the Hartmann

* Corresponding author.
E-mail address: f.fico@lboro.ac.uk (F. Fico).

https://doi.org/10.1016/j.ijheatmasstransfer.2024.125857
Received 4 September 2023; Received in revised form 30 May 2024; Accepted 12 June 2024
Available online 21 June 2024

Nomenclature

Abbreviations

DNS	Direct numerical simulation
LES	Large eddy simulation
MHD	Magnetohydrodynamic
r.m.s.	Root mean squared
SGS	Subgrid scale
WALE	Wall-adaptive local eddy viscosity

Greek, Roman and general notations

(x, y, z)	Coordinates (m)
α	Thermal diffusivity (m^2s^{-1})
β	Thermal expansion coefficient (K^{-1})
δ_b	Boundary layer thickness
δ_{ij}	Kronecker delta
ℓ_F	Lorentz force ($m\,s^{-2}$)
ϵ_{ijk}	Levi-Civita tensor
λ	Thermal conductivity ($kg\,m\,s^{-3}K^{-1}$)
ν	Kinematic viscosity (m^2s^{-1})
ϕ	Electric potential ($kg\,m^2s^{-3}A^{-1}$)
ρ	Density ($kg\,m^{-3}$)
σ	Electrical conductivity ($kg^{-1}m^{-3}s^3A^2$)
θ	Modified temperature (K)
ξ	Molecular heat flux
B_0	Imposed magnetic field ($kg\,s^{-2}/A$)
C_f	Skin friction coefficient
c_w	Wall conductivity parameter
c_p	Specific heat capacity at constant pressure ($m^2K^{-1}s^{-2}$)
D_h	Hydraulic diameter (m)
g	Acceleration of gravity (ms^{-2})
J	Electric current density ($A\,m^{-2}$)
p	Pressure ($kg\,m^{-1}s^{-2}$)
q_w	Wall heat flux ($kg\,s^{-3}$)
S_{ij}	Strain rate tensor (s^{-1})
T_f	Friction temperature (K)
t_w	Solid wall thickness (m)
T_b	Bulk temperature (K)
u, v, w	Fluid velocity ($m\,s^{-1}$)
U_b	Bulk velocity ($m\,s^{-1}$)
u_τ	Friction velocity ($m\,s^{-1}$)

Non dimensional numbers symbols

Gr	Grashof number
Ha	Hartmann number
Nu	Nusselt number
N	Stuart number
Pr	Prandtl number
Re_m	Reynolds magnetic number
Re	Reynolds number
Ri	Richardson number

Subscripts/Subscripts

$\bar{(\cdot)}$	Filtered quantity
$(\cdot)'$	Fluctuations
$(\cdot)^*$	Normalized by bulk quantities
$(\cdot)^+$	Normalized by ν, u_τ, T_f
$\langle\cdot\rangle$	Time averaged quantity

boundary layer thickness respectively. At relatively high N the flow is laminarized by the magnetic field [16,17].

Although a fundamental aspect in the design of blankets, the influence of thermal convection has only recently received more attention [18,19]. The underlying assumption was that the presence of a magnetic field at high Hartmann number values would effectively eliminate velocity fluctuations, resulting in a laminar, steady-state flow characterized by passive heat transfer. As pointed out by various studies [20–25], this is not usually the case, with the flow and heat transfer behaviour highly dependent on the flow configuration. Zhang et al. [26] found that the parameter $Gr/(HaRe) = 4$ is the threshold value for the flow instabilities in downward flows. Moreover, the experimental work of Sahu et al. [27] concluded that for horizontal ducts at $Ha > 220$ and $Ri < 10$ or $Ha > 440$ and $Ri > 10$, the buoyancy forces are superseded by magnetic field effect, while Akhmedagaev et al. [28] found persisting magnetoconvective fluctuations at $Ha \approx 1000$ and $Gr > 10^8$. Anomalous high-amplitude temperature fluctuations in mixed convection have been observed by Belyaev et al. [24] for a downward electrically insulated pipe flow at high Gr and N. Moreover, various works have tried to investigate some of the aspects of magnetoconvection within simplified or reduced blanket designs [29–33], these tried to address specific point designs or used simplified models due to the insurmountable challenges in terms of computational resources. On the other hand, the majority of studies focused on insulated solid walls (or almost insulated [34]), whereas the impact of electrically conductive walls is intricate and challenging to forecast, as it is widely recognized to alter the MHD flows [25].

In this study, another approach is followed, that emphasizes the necessity to understand the fundamental characteristics of convection in the presence of a strong magnetic field before delving into the intricate analysis of specific blanket designs. The present work is focused on the upward magnetoconvection within a square duct with finite wall conductivity. Two different thermal boundary conditions are analysed: uniform heat fluxes and one-sided heating. The one-sided heating finds practical application in various blanket designs [7,35], while the uniform heat fluxes boundary is more common in the literature, and can provide a simple comparison for understanding the mechanism of heat transfer within magnetoconvection.

The analysis reveals a complex interaction between convection and magnetic field effects. The transition from laminar to turbulent flow is partially related to the ratio of buoyancy to Lorentz forces, but also to the local reorganization of electric current density. On the other hand, the effect on heat transfer is not straightforward, and depends on the thermal boundary condition applied. When one-sided heating is applied, turbulent heat fluxes play an important role in the total heat transfer, in contrast with the typical behaviour of liquid metals and with the results of uniform heat fluxes case (at comparable Ri). Moreover, the wall conductivity parameter c_w is found to have a significant impact on the flow and heat transfer.

The remainder of this article is organized as follows. Section 2 describes the governing equations and numerical methods. Section 3 presents the results and discussion. Finally, Section 4 summarizes the main conclusions of this work.

2. Governing equations and numerical methods

The fluid is considered incompressible, electrically conductive, viscous Newtonian. Following the assumption of small Reynolds magnetic

number ($\mathrm{Re_m}$), the magnetic field affects the velocity field, and not vice-versa. In this condition, the inductionless formulation for MHD can be used. Spatially uniform and time-independent magnetic field $\boldsymbol{B} = B_0 \boldsymbol{e}_y$ is imposed in the horizontal transverse direction (y). The fluid thermophysical properties are based on the characteristic of lithium-lead [36]. These properties are considered constant within the relevant temperature range [37], as their variations are negligible. Oberbeck–Boussinesq approximation is applied, for which the variations of thermophysical properties of the fluid with pressure and temperature are neglected, except for density, for which linear variation with temperature is assumed in the buoyancy force term. Only buoyancy-assisted (upward) flows are considered. Fig. 1 shows a schematic diagram of the duct geometrical characteristics. Here x, y and z represent the axial, horizontal and vertical coordinates respectively. The Reynolds number based on the bulk velocity U_b and the hydraulic diameter (the width of square duct) D_h is $\mathrm{Re}_{D_h} = 5600$ and the Prandtl number is $\mathrm{Pr} = 0.0238$; the Hartmann number is also computed based on the hydraulic diameter. The computational length in the axial direction is $L_x = 50 D_h$. Continuity, momentum, and energy equations of the incompressible MHD flow at low magnetic Reynolds number ($\mathrm{Re_m}$) are, in Einstein's notation:

$$\frac{\partial \bar{u}_i}{\partial x_i} = 0, \tag{2}$$

$$\frac{\partial \bar{u}_i}{\partial t} + \frac{\partial}{\partial x_j}(\bar{u}_i \bar{u}_j) = -\frac{1}{\rho}\frac{\partial \bar{p}}{\partial x_i} - \frac{\partial \tau_{ij}^{sgs}}{\partial x_j} + \nu \frac{\partial^2 \bar{u}_i}{\partial x_j \partial x_j} + \mathscr{\ell}_{F_i} + f_{b_x} \tag{3}$$

$$\frac{\partial \bar{\theta}}{\partial t} + \bar{u}_j \frac{\partial \bar{\theta}}{\partial x_j} = \bar{u}_x \frac{\partial T_w}{\partial x} + \frac{\partial}{\partial x_j}\left(\alpha \frac{\partial \bar{\theta}}{\partial x_j}\right) \tag{4}$$

where the overbar indicates the spatial filtering, and u_i, p, ρ, α, represent respectively velocity vector component, pressure, density and thermal diffusivity. The velocity vector components, $\mathbf{u}(u, v, w)$ are expressed respectively in axial (x), horizontal (y) and vertical (z) directions. The term $\mathscr{\ell}_F = (1/\rho)\bar{\mathbf{J}} \times \mathbf{B}_0$ is the Lorentz force, where $\mathbf{J}$ is the electric current density. The electric density current is computed using the Ohm's law (Eq. (5)) and charge conservation (Eq. (6)) equations:

$$\bar{J}_i = \sigma\left(-\frac{\partial \bar{\phi}}{\partial x_i} + \epsilon_{ijk} \bar{u}_j B_{0_k}\right), \tag{5}$$

$$\frac{\partial \bar{J}_i}{\partial x_i} = 0 \tag{6}$$

where ϕ is the electric potential, σ is the electric conductivity of the fluid, and ϵ_{ijk} is the Levi-Civita tensor (alternating unit tensor). Combining Eqs. (5) and (6), one obtains the Poisson equation for the electric potential:

$$\frac{\partial^2 \bar{\phi}}{\partial x_i^2} = \frac{\partial}{\partial x_i}(\epsilon_{ijk} \bar{u}_j B_{0_k}) \tag{7}$$

No-slip boundary conditions are enforced at the walls for the velocity field. The subgrid-scale (SGS) stress tensor, τ_{ij}^{sgs} appears in Eq. (3) due to the filtering operation, and is defined as:

$$\tau_{ij}^{sgs} = \tau_{ij} - \frac{1}{3}\tau_{kk}\delta_{ij}, \qquad \tau_{ij} = \overline{u_i u_j} - \bar{u}_i \bar{u}_j \tag{8}$$

where δ_{ij} is the Kronecker delta. The SGS stresses are evaluated with wall-adapting local eddy-viscosity (WALE) model [38] as:

$$\tau_{ij}^{sgs} = -2\,\nu_{sgs}\,\overline{S}_{ij}, \tag{9}$$

where $\overline{S}_{ij}$ is the resolved strain rate tensor and ν_{sgs} is the SGS viscosity.

At very low Prandtl numbers there is no need for an SGS heat flux model because the grid is sufficiently fine to resolve all temperature scales [39]. Periodic boundary conditions are applied in the axial (streamwise) direction. Two different thermal boundary conditions are investigated here: uniform heat fluxes for all walls (Fig. 1b) and one-sided Hartmann heated wall (Fig. 1c). For both conditions, the modified temperature $\theta = T - T_b$ is then introduced. When uniform heat fluxes are applied, the temperature T grows in the streamwise direction. The first term on the right-hand side of Eq. (4) is defined as the constant mean axial wall temperature gradient for constant heat flux condition. Because of the uniform heat load, the time and section averaged temperature increases linearly in the streamwise direction, i.e.,

$$\frac{\partial \langle T \rangle}{\partial x} = \frac{\partial T_b}{\partial x} = \frac{\partial T_w}{\partial x} \approx const. \tag{10}$$

where T_b and T_w are the local mean bulk and wall temperature, respectively, at a given streamwise location. The latter is computed following Patankar et al. [40] as:

$$\frac{\partial T_w}{\partial x} = \frac{4 q_w}{\rho c_p U_b D_h} \tag{11}$$

where U_b is the bulk velocity and c_p is the specific heat coefficient at constant pressure. The modified temperature so defined does not grow in the streamwise direction for a fully developed flow. Different applications of this methodology can be found in various works [39]. The term $\bar{u}_x \partial T_w/\partial x$ in Eq. (4) is zero when the one-sided heating boundary is used, as there is no need for special treatment of temperature. When one-sided heating is used, the side walls (top and bottom walls of Fig. 1c) are adiabatic. Note that both thermal boundaries are applied at the solid–fluid interface, i.e. no energy equation is solved for the solid.

As mentioned at the beginning of this section, the Oberbeck–Boussinesq approximation is used, and the fluid density changes due to temperature variation

$$\rho_k = \rho_0(1 - \beta\theta) \tag{12}$$

where ρ_0 is the reference density, β is the thermal expansion coefficient. The buoyancy force is then:

$$f_{b_x} = -\rho_k g \boldsymbol{e}_x \tag{13}$$

where $\boldsymbol{e}_x$ indicates the direction of gravity (g). The Boussinesq approximation is particularly good for liquid metals, where the density change due to temperature is small. The validity of this approximation is discussed in [41]. As mentioned before, the Richardson number depends on the Grashof number that is defined as:

$$Gr = \frac{g\beta q_w D_h^4}{\nu^2 \lambda} \tag{14}$$

for four walls heating boundary (with λ representing the thermal conductivity) and as

$$Gr = \frac{g\beta \Delta T D_h^3}{\nu^2} \tag{15}$$

for one-sided heating thermal boundary.

2.1. Fluid–solid coupling

When an electrically conductive fluid is subjected to a magnetic field, and it comes into constant contact with conductive walls, there is an exchange of electric current density at the interface between the fluid and the solid walls. Numerically, the presence of solid walls is accounted for through a segregated approach. The computational domain is split into liquid and solid sub-domains, where the two are solved separately and then coupled through a boundary condition. Consequently, also for the solid, the Poisson equation is solved:

$$\nabla \cdot (\sigma_s \nabla \phi_s) = 0 \tag{16}$$

where the subscript s indicates the solid domain. Along the fluid/wall interface, the conservation and continuity of the electric current density ($\boldsymbol{J}$) needs to be kept. This is achieved by imposing the following set of boundary conditions at the interface:

$$\sigma \frac{\partial \phi}{\partial n} = \sigma_s \frac{\partial \phi_s}{\partial n} \tag{17}$$

$$\phi = \phi_s \tag{18}$$

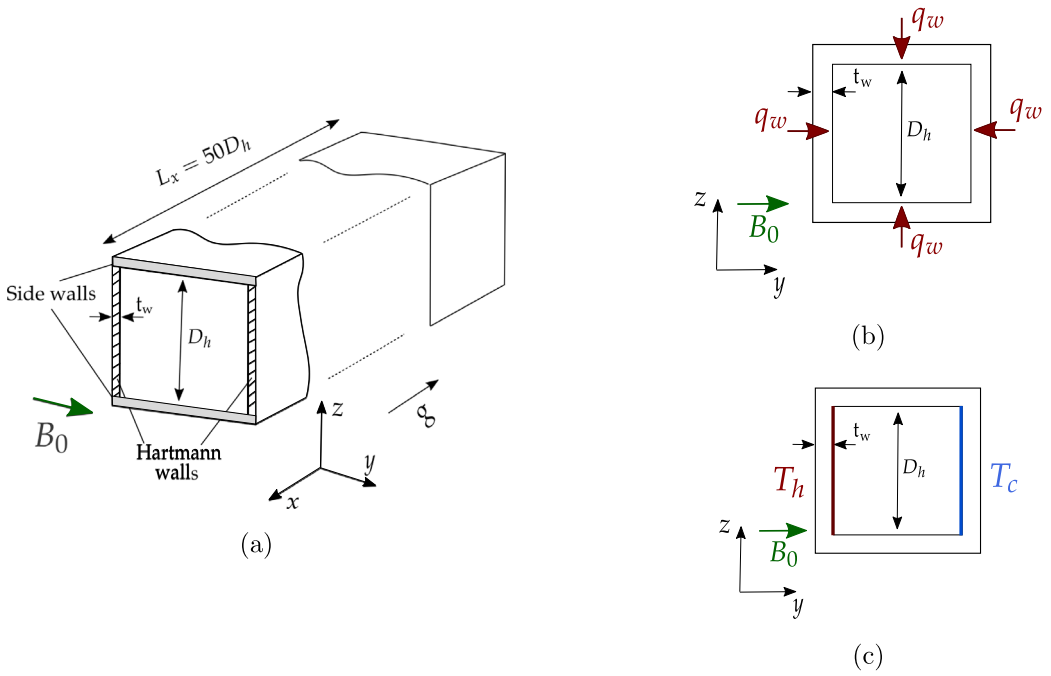

Fig. 1. Square duct (a). The magnetic field is uniform and oriented in the positive y direction. The flow is in the positive x direction. Uniform heat fluxes (b). One-sided heating (c).

Table 1
Geometrical, physical and mesh characteristics. Mesh grid spacing values normalized with mean value of friction velocity u_τ.

Data		Mesh	
Re_{D_h}	5600	$N_x\ N_y\ N_z$	(1000, 160, 124)
Pr	0.0238	Δx^+	19.5
t_w	$0.2D_h$	$\Delta y^+\|_{(min)}$	0.025
L_x	$50D_h$	$\Delta y^+\|_{(max)}$	5.625
		$\Delta z^+\|_{(min)}$	0.25
		$\Delta z^+\|_{(max)}$	5.625

The quantity of electric current density passing though the interface is controlled by the wall conductivity parameter, expressed as:

$$c_w = \frac{\sigma_s t_w}{\sigma D_h} \tag{19}$$

where t_w is the solid wall thickness. In ideal cases, when $c_w = 0$, the solid walls can be considered perfectly insulated.

2.2. Numerical methods

The simulations are carried out with an in-house version of the open source code OpenFOAM [42]. The pressure–velocity coupling is solved using PIMPLE methodology. The electric currents and Lorentz force are estimated using a conservative interpolation following Ni et al. [43] approach. The discretized equations are integrated in time with backward second order implicit scheme. The spatial discretization is made through central differences. The overall accuracy in both time and space is of 2nd order. The mesh is uniform in the axial direction, while a non-uniform spacing is used in the y and z directions, with the control volumes clustered towards the walls.

Table 1 summarizes the geometrical, physical and mesh characteristics, where N_x, N_y and N_z are the number of cells in the axial, horizontal and vertical directions. The fine resolution in the y direction is necessary to capture the electric currents closing within the thin Hartmann boundary layer, whose thickness is of the order of $\delta^* \approx 1/\mathrm{Ha}$. The temporal averages, denoted by $\langle\cdot\rangle$, are collected over a computational time of $400\,t^*$, where $t^* = D_h/U_b$ is the characteristic time. The values are then averaged spatially in the streamwise direction. For all simulations the maximum time step is imposed by imposing a maximum Courant–Friedrichs–Lewy value of 0.3. This result in a computational time step of $0.001\,t^*$. Wall coordinates, denoted using the superscript $(^+)$, are normalized using the kinematic viscosity ν and the friction velocity $u_\tau = \sqrt{\tau_w/\rho}$, where τ_w is the wall shear stress. The friction velocity is defined respectively at side walls (z) for $y/D_h = 0.5$ and Hartmann walls (y) for $z/D_h = 0.5$. When not otherwise specified, global coordinates (normalized with D_h) are used, and the subscript $(^*)$ is omitted in the next sections.

3. Results and discussion

This section aims at investigating the combined effects of magnetic field and buoyancy on the flow for two thermal boundary conditions. Due to the magnetic field presence, electric currents are generated in the fluid; which are responsible for the Lorentz force. The electric currents distribution depends on the value of electrical conductivity parameter (c_w), which determines if the electric currents enter or not the solid walls. This highly affects the flow behaviour, as different electric current density implies different Lorentz forces distribution. Validation of the numerical approach and of the solver is discussed in the appendix of [39]. Following, Section 3.1 presents the results for uniform heat fluxes, while Section 3.2 for one-sided Hartmann wall heating. Note that in the following sections, the line plots shown are collected along the y direction at $z = 0.5$, and along the z direction at $y = 0.5$, unless otherwise specified.

3.1. Flow structure and temperature field for uniform heat fluxes

For the uniform wall heating case, one would expect the flow to be drifted upwards by the buoyancy forces. A summary of the cases studied is presented in Table 2. The flow structure is qualitatively shown in Figs. 2a and 2b, where the instantaneous axial velocity and near-wall streamwise streaks are plotted for an arbitrary time. Due to the buoyancy forces, jet-like structures are observed at the four corners of the duct. For the magnetoconvective case (Fig. 2a), the axial velocity

Table 2
Case studied at uniform heat fluxes and one-sided heating. Re ≈ 5602, Pr ≈ 0.0238.

Uniform heat fluxes						
Ha	0	45	125	125	125	125
Ri	10	2.8	5	10	10	10
c_w	-	0.05	0.05	0.01	0.05	0.5
symbols/lines	———	---●---	·····	–·–○–·–	–·–△–·–	–·–□–·–
Case name	A1	E3	C3	D2	D3	D4
One-sided heating						
Ha		95	95	125	9.4	125
Ri		6.2	7.5	7.5	8.5	9.5
c_w		0.05	0.05	0 .05	0.05	0.05
ΔT		50	60	60	70	80
symbols/lines		———	·····	–·–○–·–	–·–△–·–	–·–□–·–
Case name		G1	H1	H2	I2	J2

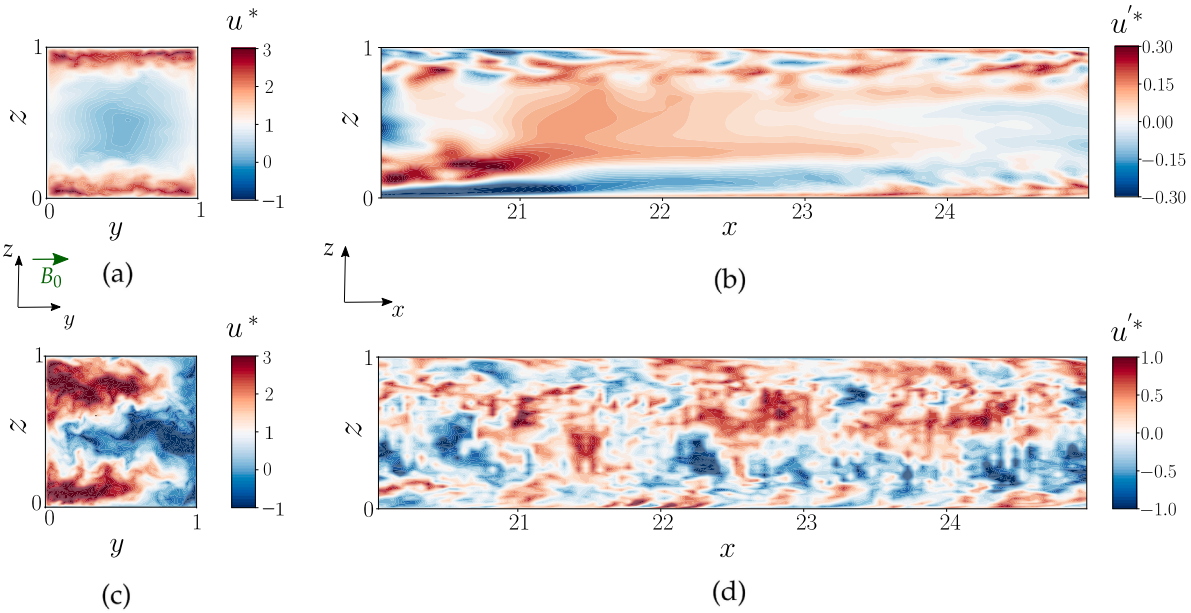

Fig. 2. Instantaneous normalized axial velocity ($u^* = u/U_b$), and streamwise streaks at $y^+ \approx 21$. (a - b) uniform heating case (Ha = 125, Ri = 10 and $c_w = 0.05$), and (c - d) one-sided heating (Ha = 125, Ri = 9.5 and $c_w = 0.05$). Flow in positive x direction.

is accelerated at the entire side walls, while smaller velocities are observed at the Hartmann wall. Fig. 2b shows how the near wall turbulent structures tend to be suppressed around the centreline close to the Hartmann wall. The flow velocity decreases in the core of the duct, due to both negative buoyancy and Lorentz force. Similar conclusions are inferred by looking at Fig. 3, where it can be observed that the mean axial velocity in the z direction is affected by the local electric current distribution, and that the maximum velocity is correlated to the growth of c_w on the side wall. This is not observed in the y direction. Contrary to the purely MHD case, the jet-like structures are also present on the Hartmann walls. The velocity profiles can be partially explained by the distribution of the electric current density, shown in Fig. 4. This differs from the typical distribution observed in the purely magnetohydrodynamic case [44]. In D2 and D3 the electric currents form two large loops in the core of the duct, for which the isoline distribution depends on the wall conductivity parameter. At low c_w the electric currents are clustered towards the Hartmann walls. Increasing c_w, the electric currents almost fully enter the solid walls as shown in Fig. 4c. These features indicate alterations of the flow structure due to the presence of Lorentz and buoyancy forces. Further insight is provided by the analysis of the interaction of these forces with turbulence. In Fig. 5, the root mean squared (r.m.s.) of velocity fluctuations are shown. The magnetoconvective (cases C3, D2–D4 of Table 2) r.m.s. of velocity fluctuations have smaller amplitude compared to the A1 case. This is particularly true for the y direction, where the fluctuations are highly suppressed and approach zero for $v^+_{r.m.s}$ and $w^+_{r.m.s}$ (Figs. 5c and 5e). At $c_w \approx 0.01$ the level of fluctuations is somewhat larger than all the other cases. This is linked to the turbulence suppression being less effective at low c_w values. It is important to point out that along the z direction, the level of r.m.s velocity is comparable or higher than the purely hydrodynamic case [45]. This is most likely related to an increment of

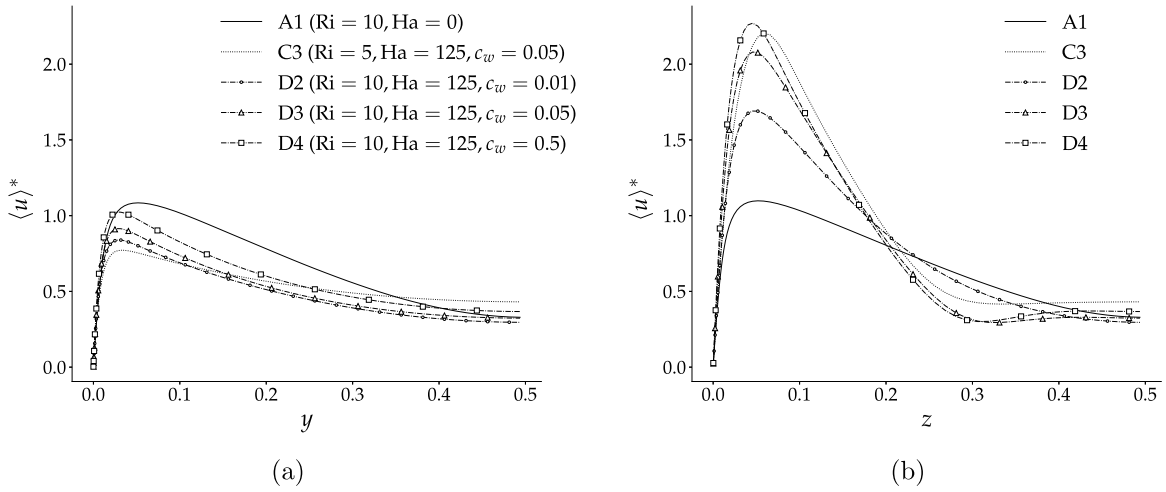

Fig. 3. Mean axial velocity at Ri ≈ 10 and uniform heat fluxes. (a) along the y direction, (b) along the z direction.

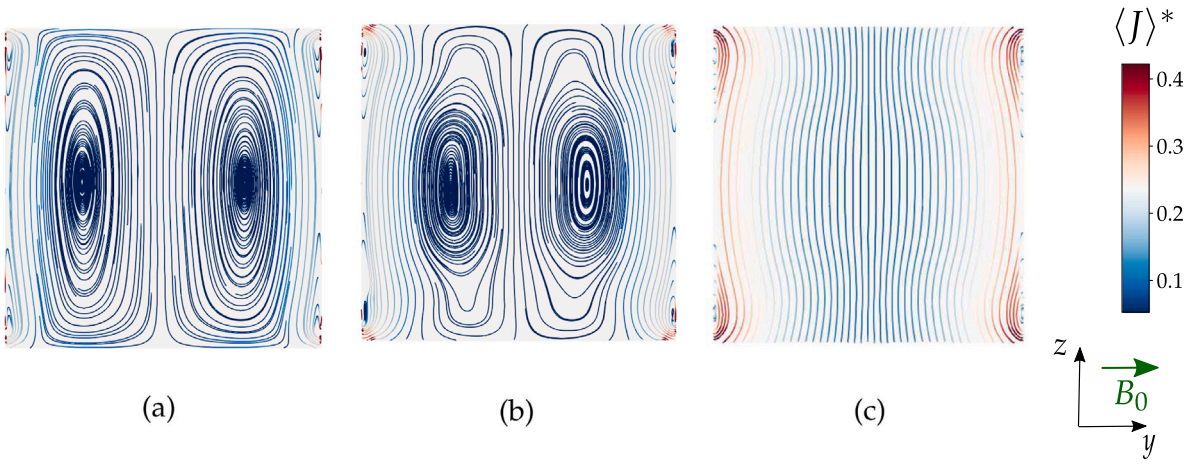

Fig. 4. Axial section of normalized electric current density distribution at Ha = 125, Ri = 10. (a) D2 (c_w = 0.01), (b) D3 (c_w = 0.05), (c) D4 (c_w = 0.5). With $\langle J \rangle^* = J/(\sigma U_b B_0)$.

a secondary flow observed to appear due to large convective motions close to the walls and to the corners presence [46,47].

A closer examination of the velocity fluctuations (Fig. 5) also indicates the suppression of the turbulent heat fluxes. Indeed, from Figs. 6a and 6b, it is quite clear that for most of the magnetoconvective cases (cases D3 and D4 in Table 2), the axial turbulent heat fluxes $\langle u'\theta' \rangle^+$ are suppressed, especially along the y direction. Along the z direction, the turbulent heat fluxes are slightly larger, but still less than 30% of the purely mixed convection (case A1 in Table 2). The lowest values are observed for the case C3 of Table 2 (not shown here), where the heat fluxes are almost zero, due to the minimal impact of the buoyancy forces. The maximum of the turbulent heat fluxes for the magnetoconvective cases are observed for the case D2 of Table 2 (Ri = 10 and c_w = 0.01), indicating the beneficial effect of a low wall conductivity parameter to the total heat transfer.

The previous analysis is confirmed by looking at the total heat fluxes in Figs. 6c and 6d. This is given by the sum of the molecular and orthogonal turbulent heat fluxes, with the molecular heat flux along y computed as:

$$\xi_y = \frac{1}{\mathrm{Pr}} \left(\frac{\partial \langle \theta \rangle}{\partial y} \right)^+ \tag{20}$$

and accordingly along the z. As shown in the figures, the turbulent heat fluxes have not a significant contribution to the total heat flux for cases D2, D3 and D4 of Table 2. Moreover, the molecular heat flux is very similar for these cases, with some variation observed among the Ri = 5 and Ri = 10 cases, due to the wider alteration of the flow structure due to buoyancy forces. This is, however, noticeable only along the (y) direction.

The results seem to confirm that the heat transfer tends to be mostly conductive when the magnetic field is strong enough. Indeed, at lower Hartmann number, the turbulent heat fluxes are not negligible. This statement is confirmed by looking at case E3 in Fig. 6, where the E3 case is the configuration at Ha = 45, c_w = 0.05 and Ri = 2.8. Further quantitative data is provided by Table 3, where the skin friction (C_f), the Nusselt number (Nu), and pressure drop are reported. The Nusselt number is calculated as follow:

$$\mathrm{Nu} = -\frac{D_h}{\langle \theta \rangle} \frac{\partial \langle \theta \rangle}{\partial y} \bigg|_{y=0} \tag{21}$$

in the y direction and accordingly in the z direction. While the pressure drop $(dp/dx)^*$ (see [16] for further description), normalized with $\frac{1}{2}\rho U_b^2/D_h$, includes viscous friction, MHD and buoyancy associated losses. The Nu values are consistent with the previous analysis, showing that Nu along the z direction is approximately twice the value along y direction. The pressure drop increases dramatically with the wall conductivity parameter.

Overall, the analysis above shows that the increase of the wall conductivity parameter negatively affects the turbulent heat fluxes, due to the more effective turbulence suppression. It is shown that for uniform heat flux boundary and under the conditions studied, heat transfer in liquid metals is predominantly diffusive, i.e. the turbulent heat fluxes

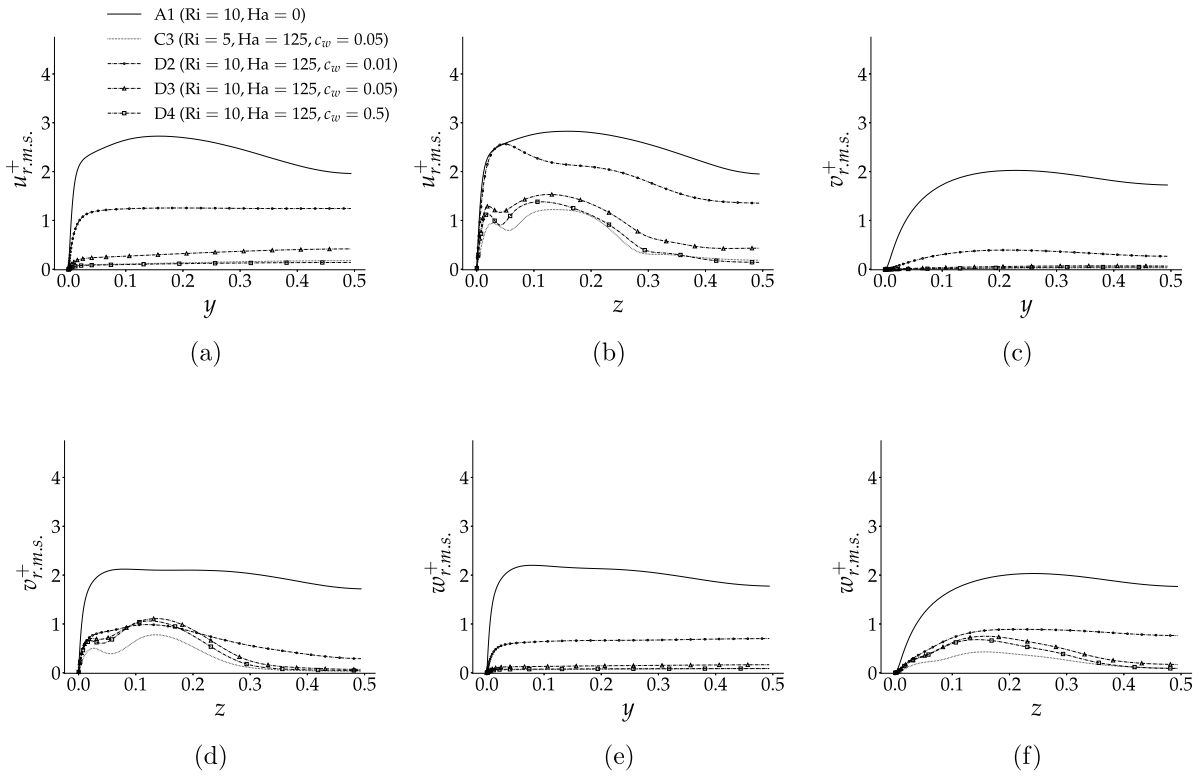

Fig. 5. r.m.s. of velocity fluctuations. (a), (c), (e) along y direction, (b), (d), (f) along z direction.

Table 3
Skin friction and Nusselt number along y and z, and normalized pressure drop for the cases with uniform heat fluxes.

Case name	A1	C3	D2	D3	D4
$C_f(y)$	0.0318	0.0369	0.0415	0.0451	0.0505
$C_f(z)$	0.0318	0.0330	0.035	0.0424	0.0485
$Nu(y)$	9.20	4.43	5.17	4.94	4.95
$Nu(z)$	9.20	9.47	9.78	10.67	10.34
$(dp/dx)^*$	0.97	1.67	1.96	2.09	4.41

are mostly negligible. This is only true for strong magnetic fields, as case E3 of Table 2 (low Ha number) indicates that the turbulent heat fluxes can be large, in contrast to the typical behaviour of low Prandtl number fluids. It will be seen in Section 3.2 that this behaviour is not observed for the one-sided heating boundary condition.

3.2. Flow structure and temperature field for one-sided heating

In the previous section, the flow and temperature structures have been analysed for uniform heat fluxes boundary condition. In this section, one sided heating boundary condition is used. As mentioned before, this configuration finds practical application in a nuclear fusion reactor blanket. The list of cases studied can be found in Table 2. The Ri has here been calculated based on the two Hartmann walls temperature difference (with Grashof number specified as in Section 2). As before, snapshots of the instantaneous axial velocity are shown in Fig. 2c. Jet-like structures are observed at the top and bottom (z direction) corners of the duct, while reversed flow is observed at the cold wall. Compared to the four-wall heating, the near wall streamwise streaks permeate the duct at every z location, and do not seem to be affected by suppression close to the Hartmann wall, as shown in Fig. 2d. Following, the mean axial velocity profile is further shown in Fig. 7. Along z (Fig. 7b), a modified MHD "M" shape is observed, with reversed flow only observed at the centre of the duct for the magnetoconvective cases. On the other hand, along the y direction (Fig. 7a), the largest axial velocity appears for the laminar case H2 of Table 2, with the inversion point (the point where algebraic sign changes) located at 80% of the y direction, while for all the other cases the inversion point is located closer to the heated wall. This behaviour is linked to the temperature distribution, shown in Fig. 8. The mean temperature is normalized against the half gap temperature $\delta T = (T_h - T_c)/2$. Along the y direction (Fig. 8a), for the laminar case H2 of Table 2, the temperature decreases linearly from the "hot" to the "cold" wall, with the inversion point located exactly at the centre of the duct ($y = 0.5$). This is not observed for all the other cases, where the temperature decays faster, with the inversion point located closer to the heated wall. These profiles suggest a significant effect of the convective turbulent motion on the temperature distribution, and with the temperature deviating from the laminar linear distribution observed for case H2 in Fig. 8a. On the other hand, the temperature variation along the z direction is much smaller, and approaches zero in the laminar case, as shown in Fig. 8b. Similarly to Section 3.1, the effects on turbulence is analysed by looking at the r.m.s of velocity fluctuations, shown in Fig. 9.

Differently from the previous configuration, the r.m.s. of velocity fluctuations are large for all turbulent cases, and except for the laminar case (case H2 of Table 2), their amplitude is quite high for both y and z directions. Along the y direction, for all three main components ($u'^+_{r.m.s.}$, $v'^+_{r.m.s.}$ $w'^+_{r.m.s.}$), the largest values are consistently observed for the case G1 of Table 2, with the amplitude decreasing as Ri/Ha decreases. Along the z direction, instead, the largest values are observed for case J2, with G1 and H1 cases (Table 2) exhibiting an almost perfect overlap, implying that the amplitude of r.m.s at this location might be more dependent on the Hartmann number than the Richardson number. Moreover, there is a substantial difference between cases H2 and J2, and no intermediate states between the laminar and turbulent cases are observed. The previous analysis indicates a strong turbulence presence for one-sided heating boundary condition. This reflects on the turbulent heat fluxes, as shown in Fig. 10a. As opposed to the uniform heat fluxes case, the turbulent heat fluxes are not negligible and represent a significant portion of the total heat fluxes. Furthermore, it can be

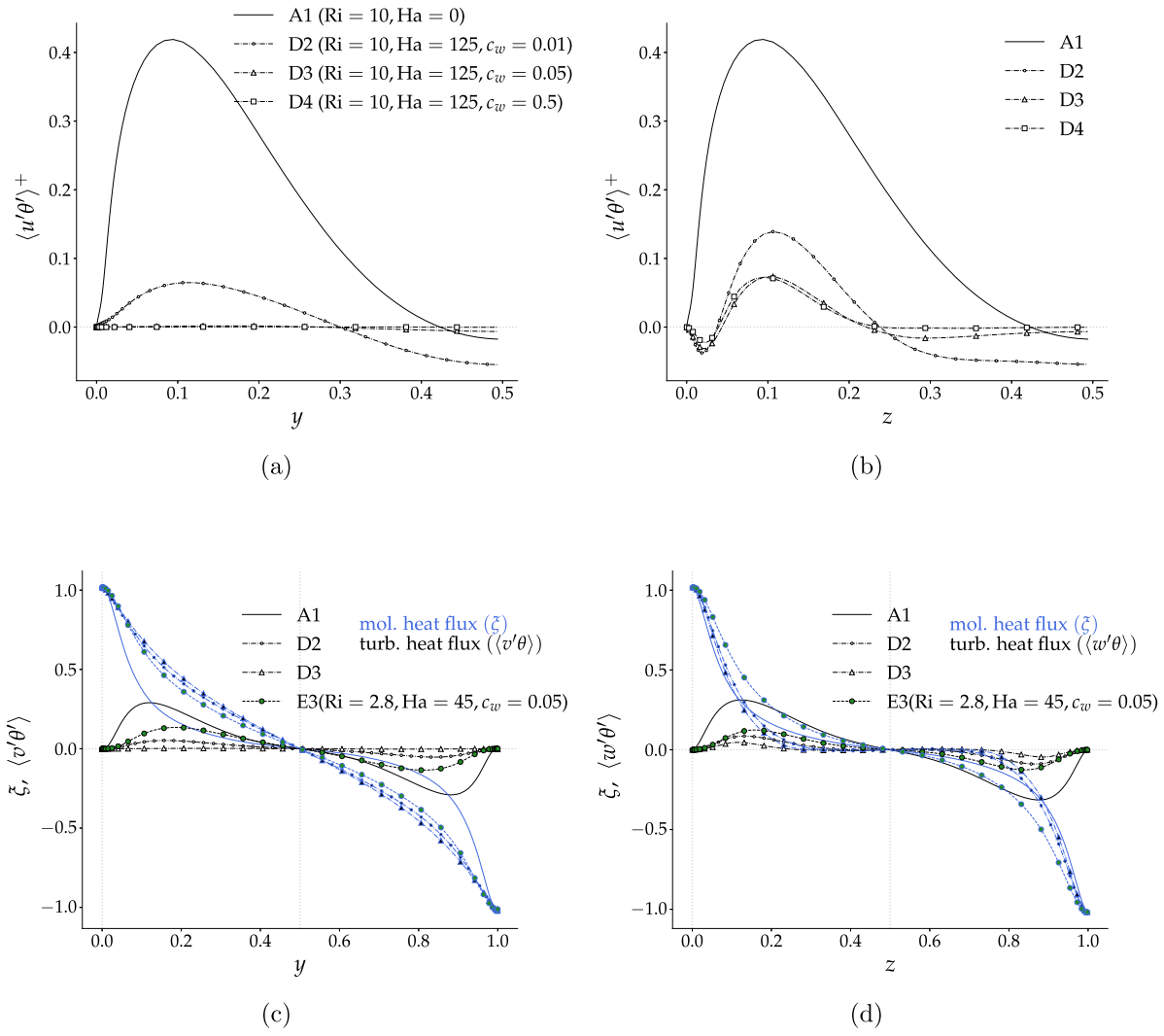

Fig. 6. Axial turbulent heat fluxes along y (a) and along z(b); normal turbulent and molecular heat fluxes along y (c) and z (b).

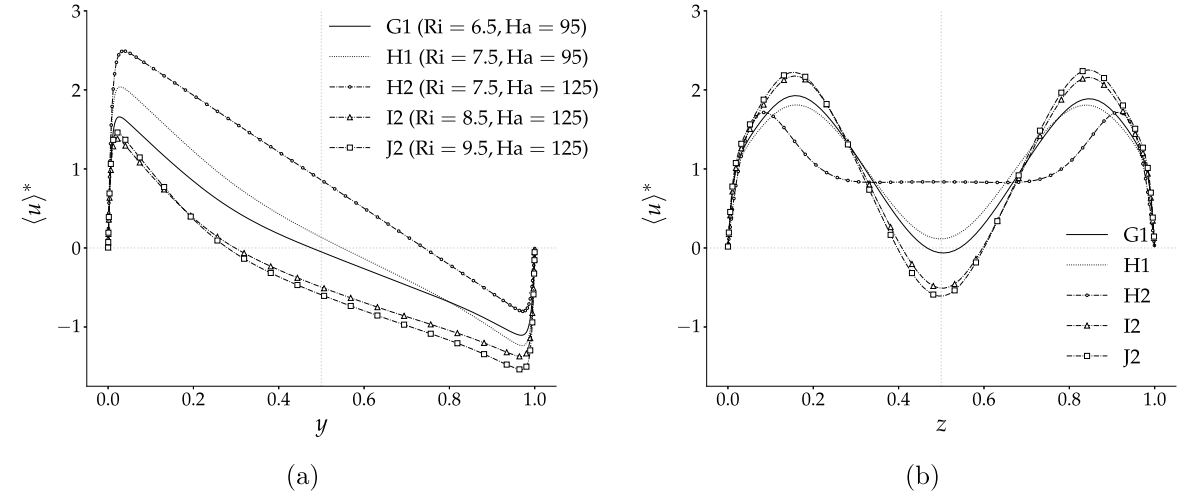

Fig. 7. Mean axial velocity. (a) along the y direction, (b) along the z direction for one-sided heating.

noticed that the molecular heat fluxes are almost equal amongst all the cases shown in Fig. 10a (cases G1, I2 and J2 of Table 2), and thus the variation of the total heat fluxes is only due to the turbulent heat fluxes. The latter are smaller going from J2 and I2 cases to G1 case. This indicates a detrimental effect of a large magnetic on the turbulent heat fluxes. Similar results to G1 are obtained for the case H1 (not shown here). The contribution to total heat fluxes is also clear by looking at Fig. 10b, where the Nusselt number variation along the Hartmann "hot"

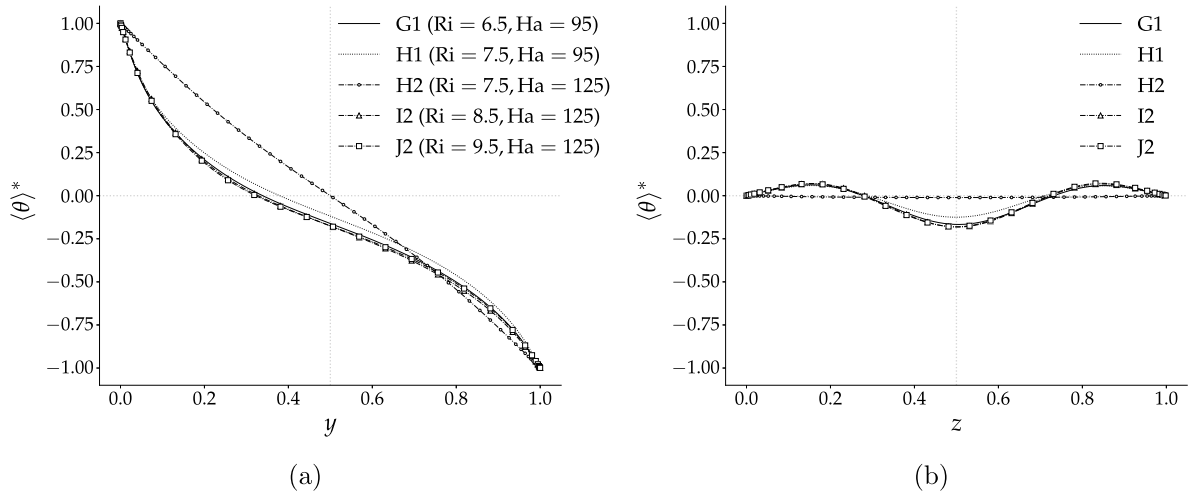

Fig. 8. Mean temperature for one sided heating. (a) along y direction, (b) along z direction.

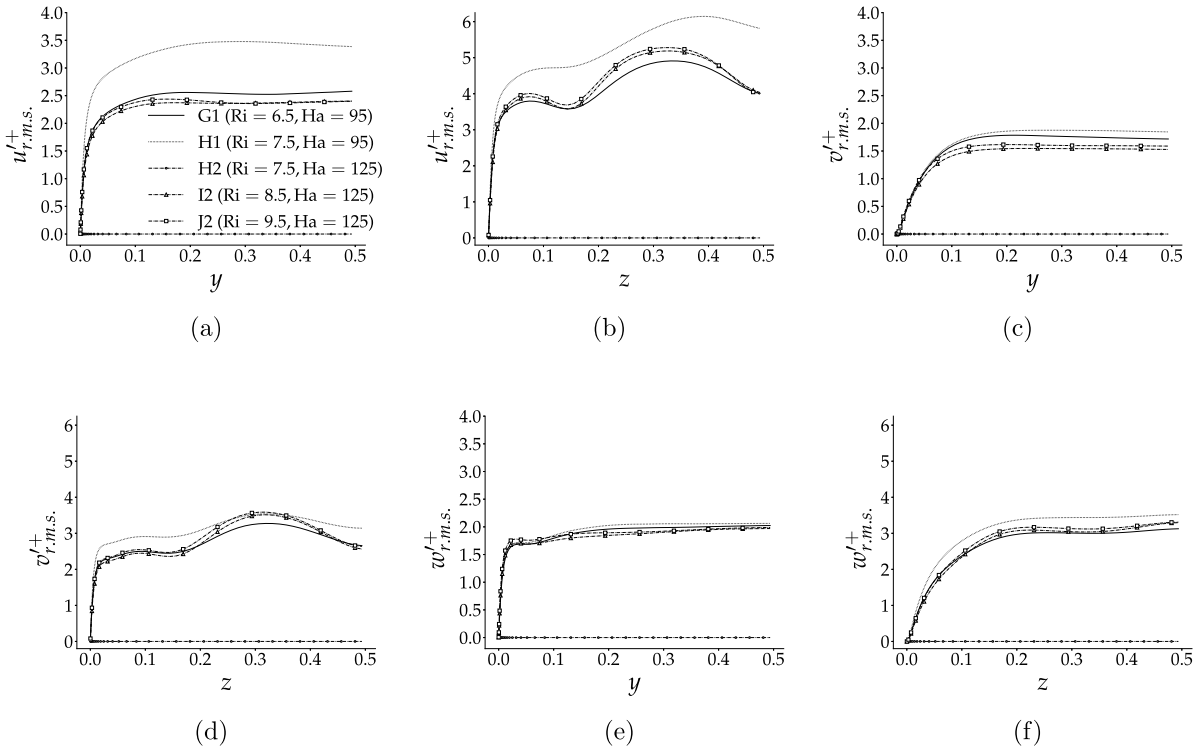

Fig. 9. r.m.s. of velocity fluctuations. (a), (c), (e) along the y direction, (b), (d), (f) along the z direction.

wall ($y = 0$) is shown. It is worth noting that for case H2, the Nusselt number is four times smaller than all the other cases, confirming the complete suppression of the convective motion for this case.

Overall, the results show the flow restructuring by the combined effect of the magnetic field and thermal convective motion. The wall conductivity parameter plays an important role in alignment, or deviation from it, of the Lorentz force with the buoyancy forces, i.e., instabilities and flow configuration are highly dependent on various factors, such as magnetic field orientation, wall conductivity parameter, type of thermal boundary condition, and direction of gravity vector. For one-sided heating, the results show that the turbulent heat fluxes are not negligible, and provide a good portion of the total heat transfer. Moreover, the different ways in which the thermal structures are affected when using uniform or one-sided boundary conditions is an indication of the complex nature of the interaction between the magnetic field and the buoyancy forces. This difference is further noticeable in Fig. 11, where the temperature variance production term $P_\theta = -\langle v'\theta'\rangle d\langle\theta\rangle/dy$ is shown for the two thermal boundary conditions. Indeed, for the one-sided heating case, the turbulent temperature structures deviate from the typical ones observed in liquid metals. As qualitatively shown in Fig. 12, the temperature structures in Fig. 12a (forced convection) are larger and less perturbed compared to the ones in Fig. 12b, where finer and more detailed scales can be noticed.

4. Conclusions

In this work a numerical study of the turbulence, heat transfer and magnetic field interaction has been presented for a square duct. Two thermal boundary conditions have been investigated: uniform heat fluxes, and one-sided heating. It has been found that at specific

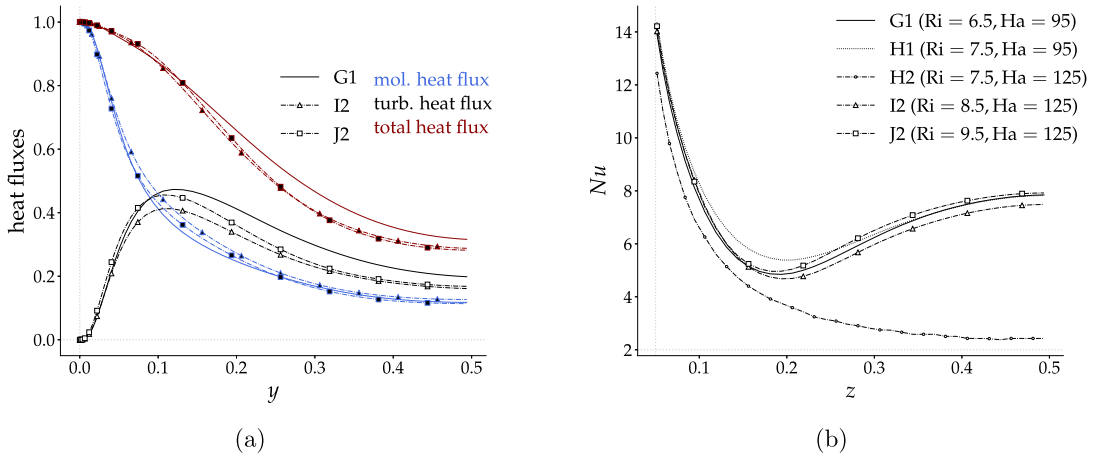

Fig. 10. Total, molecular and turbulent heat fluxes along the y direction (a) and local Nu variation along the z direction at $y = 0$ (b).

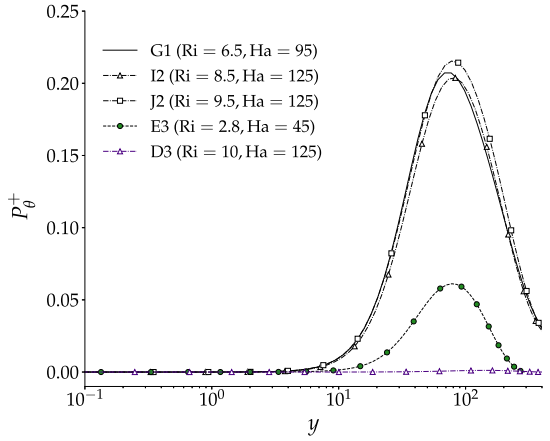

Fig. 11. Production term of temperature variance along the y direction. Comparison between one-sided heating and uniform heat fluxes boundary conditions.

Ri/Ha values the flow transitions to turbulent, partially due to the local reorganization of the electric currents. Moreover, the two boundary conditions used show that the state of the flow and heat transfer characteristics cannot be determined by merely accounting for the magnitude of the Ri, Re and Ha numbers, but also depends on the wall conductivity parameter and the local thermal boundaries. In summary:

(i) for the configuration studied, low c_w is beneficial for the increment of turbulent heat fluxes, and consequently, of the total heat fluxes;
(ii) the turbulent and thermal structures are highly dependent on the thermal boundary conditions, which completely alter the flow structure;
(iii) at parity of Ri values, for one sided heating, the turbulent heat fluxes can become large and significantly contribute to the total heat transfer, in contrast to the uniform heat fluxes case and to the typical behaviour of low Prandtl number fluids.

Overall, this work highlights some of the liquid metals features within magnetic fields and the buoyancy forces, and provides quantitative data about their heat transfer characteristics. These indicate that the use of liquid metals in nuclear fusion reactors, will necessitate further investigations to thoroughly understand the physical systems and its effects on behaviour of such systems. Potential extensions could include different flow configurations, off-design conditions, as unsteady and non-uniform magnetic field, and variable electric wall conductivity.

CRediT authorship contribution statement

Francesco Fico: Writing – review & editing, Writing – original draft, Visualization, Software, Methodology, Investigation, Formal analysis, Conceptualization. **Hao Xia:** Writing – review & editing, Supervision, Project administration, Methodology, Conceptualization. **Ivan Langella:** Writing – review & editing, Supervision, Methodology, Funding acquisition, Conceptualization. **Gerasimos Politis:** Writing – review & editing, Supervision, Methodology.

Declaration of competing interest

The authors declare that they have no known competing financial interests or personal relationships that could have appeared to influence the work reported in this paper.

Data availability

Data will be made available on request.

Acknowledgements

The authors acknowledge the funding support from Engineering and Physical Science Research Council (EPSRC), United Kingdom under Grant No. EP/R513088/1 and UK Atomic Energy Authority (UKAEA). The authors are grateful for the use of Lovelace HPC at Loughborough University, Sulis Tier-2 at HPC Midlands+, and UK's national facility ARCHER2 via the UK Turbulence Consortium (Grant No. EP/R029 326/1).

Appendix A. Mesh resolution

In Section 2 it was mentioned that the mesh is fine enough to resolve all the thermal scales, i.e. no sub-grid scale term is necessary. The velocity field scales are linked to the Kolmogorov length scale, $\eta = (\nu^3/\varepsilon)^{1/4}$, with ε being the dissipation rate of turbulent kinetic energy, and the Obukhov–Corrsin length scale is the one for the temperature field, $\eta_T = \eta Pr^{-3/4}$. As one can notice in Fig. A.13a the LES filter width $\Delta = \sqrt[3]{\mathcal{V}_{\text{cell}}}$ ($\mathcal{V}_{\text{cell}}$ is the cell volume), is significantly smaller than η_T, indicating that thermal structures are predicted with DNS resolution. Moreover, in Figs. A.13b–c, the ratio of resolved k_{res} versus total $(k_{res} + k_{sgs})$ turbulent kinetic energy is presented, with k_{sgs} indicating the subgrid scale kinetic energy estimated as $k_{sgs} = \nu_{sgs}^2/(C_k\Delta)^2$, where $C_k = 0.094$ is a constant. As shown in the figure, the minimum ratio is around 96%, indicating a high resolution of the turbulent scales.

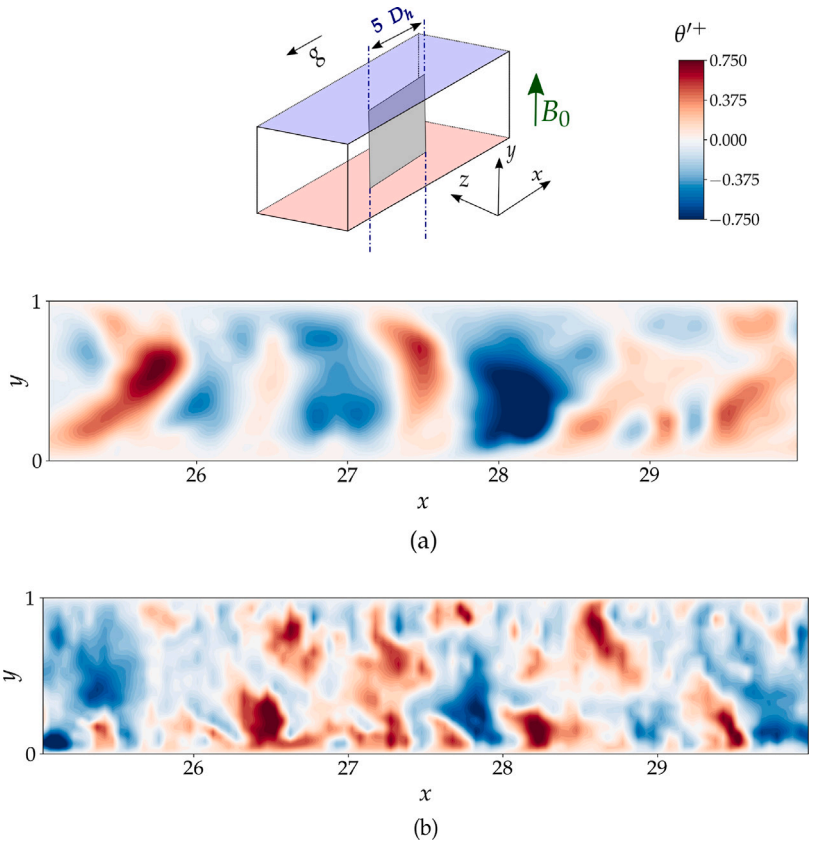

Fig. 12. Modified temperature fluctuation θ', slice along z direction. Forced convection (a), Case G1 of Table 2 (b). Flow in positive x direction.

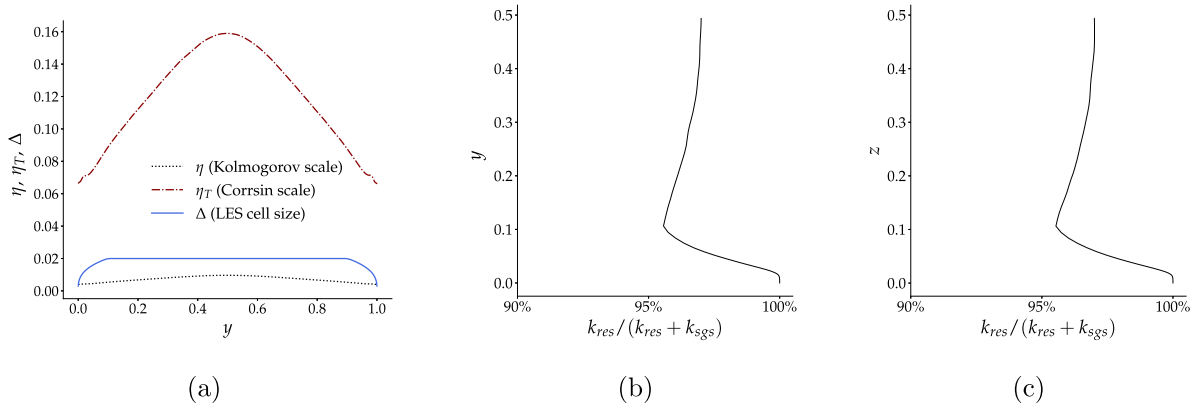

Fig. A.13. LES mesh resolution compared with Kolmogorov and Obukhov–Corrsin scale (a); Percentage of resolved to total turbulent kinetic energy along y (b) and z (c).

Appendix B. Supplementary data

Supplementary material related to this article can be found online at https://doi.org/10.1016/j.ijheatmasstransfer.2024.125857.

References

[1] I.R. Kirillov, C.B. Reed, L. Barleon, K. Miyazaki, Present understanding of MHD and heat transfer phenomena for liquid metal blankets, Fusion Eng. Des. 27 (1995) 553–569, http://dx.doi.org/10.1016/0920-3796(95)90171-x.

[2] M. Abdou, N.B. Morley, S. Smolentsev, A. Ying, S. Malang, A. Rowcliffe, M. Ulrickson, Blanket/first wall challenges and required R & D on the pathway to DEMO, Fusion Eng. Des. 100 (2015) 2–43, http://dx.doi.org/10.1016/j.fusengdes.2015.07.021.

[3] Blanket Comparison and Selection Study, Tech. Rep., Argonne National Lab. IL (USA), aNL/FPP/83-1Volume, 1984.

[4] S. Malang, J. Reimann, H. Sebening, L. Barleon, E. Bogusch, E. Bojarsky, H. Borgstedt, L. Buehler, V. Casal, H. Deckers, H. Feuerstein, U. Fischer, G. Frees, H. Graebner, H. John, T. Jordan, W. Kramer, R. Krieg, L. Lenhart, S. Malang, R. Meyder, P. Norajitra, J. Reimann, A. Schwenk-Ferrero, H. Schnauder, R. Stieglitz, J. Oschinski, E. Wiegner, Status Report KFK Contribution to the Development of Demo-Relevant Test Blankets for Net/iter, Part 1: Self-Cooled Liquid Metal Breeder Blanket. 1: Summary, Tech. Rep., 1991, http://dx.doi.org/10.5445/IR/270031466.

[5] J. Reimann, L. Barleon, I. Bucenieks, L. Bühler, L. Lenhart, S. Malang, S. Molokov, I. Platnieks, R. Stieglitz, Magnetohydrodynamic investigations of a self-cooled pb-17li blanket with poloidal-radial-toroidal ducts, Fusion Eng. Des. 27 (1995) 593–606, http://dx.doi.org/10.1016/0920-3796(95)90174-4.

[6] K.S. Malang, Dual Coolant Blanket Concept, Tech. Rep., Kern-forschugszentrum Karlsruhe, 1994.

[7] S. Smolentsev, N.B. Morley, M.A. Abdou, S. Malang, Dual-coolant lead lithium (DCLL) blanket status and RD needs, Fusion Eng. Des. 100 (2015) 44–54, http://dx.doi.org/10.1016/j.fusengdes.2014.12.031.

[8] L. Boccaccini, L. Giancarli, G. Janeschitz, S. Hermsmeyer, Y. Poitevin, A. Cardella, E. Diegele, Materials and design of the European DEMO blankets, J. Nucl. Mater. 329–333 (2004) 148–155, http://dx.doi.org/10.1016/j.jnucmat.2004.04.125.

[9] C. Mistrangelo, L. Bühler, C. Koehly, H.-J. Brinkmann, Influence of modifications of HCLL blanket design on MHD pressure losses, Fusion Eng. Des. 124 (2017) 948–952.

[10] E. Martelli, G. Caruso, F. Giannetti, A.D. Nevo, Thermo-hydraulic analysis of EU DEMO WCLL breeding blanket, Fusion Eng. Des. 130 (2018) 48–55, http://dx.doi.org/10.1016/j.fusengdes.2018.03.030.

[11] A.D. Nevo, P. Arena, G. Caruso, P. Chiovaro, P.D. Maio, M. Eboli, F. Edemetti, N. Forgione, R. Forte, A. Froio, F. Giannetti, G.D. Gironimo, K. Jiang, S. Liu, F. Moro, R. Mozzillo, L. Savoldi, A. Tarallo, M. Tarantino, A. Tassone, M. Utili, R. Villari, R. Zanino, E. Martelli, Recent progress in developing a feasible and integrated conceptual design of the WCLL BB in EUROfusion project, Fusion Eng. Des. 146 (2019) 1805–1809, http://dx.doi.org/10.1016/j.fusengdes.2019.03.040.

[12] G. Grötzbach, Challenges in low-Prandtl number heat transfer simulation and modelling, Nucl. Eng. Des. 264 (2013) 41–55, http://dx.doi.org/10.1016/j.nucengdes.2012.09.039.

[13] H.K. Moffatt, On the suppression of turbulence by a uniform magnetic field, J. Fluid Mech. 28 (03) (1967) 571, http://dx.doi.org/10.1017/s0022112067002307.

[14] P.A. Davidson, An Introduction to Magnetohydrodynamics, Cambridge University Press, Cambridge New York, 2001, http://dx.doi.org/10.1017/CBO9780511626333.

[15] J. Sommeria, R. Moreau, Why, how, and when, MHD turbulence becomes two-dimensional, J. Fluid Mech. 118 (1982) 507, http://dx.doi.org/10.1017/s0022112082001177.

[16] S. Smolentsev, Physical background, computations and practical issues of the magnetohydrodynamic pressure drop in a fusion liquid metal blanket, Fluids 6 (3) (2021) 110, http://dx.doi.org/10.3390/fluids6030110.

[17] O. Zikanov, D. Krasnov, T. Boeck, A. Thess, M. Rossi, Laminar-turbulent transition in magnetohydrodynamic duct, pipe, and channel flows, ASME. Appl. Mech. Rev. 66 (3) (2014) http://dx.doi.org/10.1115/1.4027198.

[18] H.M.S. Molokov, R. Moreau, Magnetohydrodynamics: Historical Evolution and Trends, Springer Nature, 2007.

[19] O. Zikanov, D. Krasnov, T. Boeck, S. Sukoriansky, Decay of turbulence in a liquid metal duct flow with transverse magnetic field, J. Fluid Mech. 867 (2019) 661–690, http://dx.doi.org/10.1017/jfm.2019.171.

[20] X. Zhang, O. Zikanov, Mixed convection in a horizontal duct with bottom heating and strong transverse magnetic field, J. Fluid Mech. 757 (2014) 33–56, http://dx.doi.org/10.1017/jfm.2014.473.

[21] X. Lv, O. Zikanov, Mixed convection in horizontal duct flow with transverse magnetic field and heating of side wall, Phys. Fluids 26 (9) (2014) 097106, http://dx.doi.org/10.1063/1.4896299.

[22] O. Zikanov, Y. Listratov, Numerical investigation of MHD heat transfer in a vertical round tube affected by transverse magnetic field, Fusion Eng. Des. 113 (2016) 151–161, http://dx.doi.org/10.1016/j.fusengdes.2016.10.017.

[23] I. Melnikov, E. Sviridov, V. Sviridov, N. Razuvanov, Experimental investigation of MHD heat transfer in a vertical round tube affected by transverse magnetic field, Fusion Eng. Des. 112 (2016) 505–512, http://dx.doi.org/10.1016/j.fusengdes.2016.06.003.

[24] I. Belyaev, P. Sardov, I. Melnikov, P. Frick, Limits of strong magneto-convective fluctuations in liquid metal flow in a heated vertical pipe affected by a transverse magnetic field, Int. J. Therm. Sci. 161 (2021) 106773, http://dx.doi.org/10.1016/j.ijthermalsci.2020.106773.

[25] O. Zikanov, I. Belyaev, Y. Listratov, P. Frick, N. Razuvanov, V. Sviridov, Mixed convection in pipe and duct flows with strong magnetic fields, Appl. Mech. Rev. 73 (1) (2021) http://dx.doi.org/10.1115/1.4049833.

[26] X. Zhang, O. Zikanov, Convection instability in a downward flow in a vertical duct with strong transverse magnetic field, Phys. Fluids 30 (11) (2018) 117101, http://dx.doi.org/10.1063/1.5048286.

[27] S. Sahu, C. Courtessole, A. Ranjan, R. Bhattacharyay, T. Sketchley, S. Smolentsev, Thermal convection studies in liquid metal flow inside a horizontal duct under the influence of transverse magnetic field, Phys. Fluids 32 (6) (2020) 067107, http://dx.doi.org/10.1063/5.0006260.

[28] R. Akhmedagaev, O. Zikanov, Y. Listratov, Magnetoconvection in a horizontal duct flow at very high hartmann and grashof numbers, J. Fluid Mech. 931 (2021) http://dx.doi.org/10.1017/jfm.2021.987.

[29] Z.-H. Liu, L. Chen, M.-J. Ni, N.-M. Zhang, Effects of magnetohydrodynamic mixed convection on fluid flow and structural stresses in the DCLL blanket, Int. J. Heat Mass Transfer 135 (2019) 847–859, http://dx.doi.org/10.1016/j.ijheatmasstransfer.2019.02.019.

[30] T.J. Rhodes, G. Pulugundla, S. Smolentsev, M. Abdou, 3D modelling of MHD mixed convection flow in a vertical duct with transverse magnetic field and volumetric or surface heating, Fusion Eng. Des. 160 (2020) 111834, http://dx.doi.org/10.1016/j.fusengdes.2020.111834.

[31] A. Tassone, G. Caruso, Computational MHD analyses in support of the design of the WCLL TBM breeding zone, Fusion Eng. Des. 170 (2021) 112535, http://dx.doi.org/10.1016/j.fusengdes.2021.112535.

[32] A. Khodak, A. Brooks, T. Brown, J. Klabacha, B. Linn, T. Looby, J. Menard, C. Swanson, P. Titus, H. Zhang, Virtual prototyping of liquid metal blanket performance in fusion pilot plant, Fusion Eng. Des. 191 (2023) 113692, http://dx.doi.org/10.1016/j.fusengdes.2023.113692.

[33] S. Siriano, F.R. Urgorri, A. Tassone, G. Caruso, 3D MHD analysis of prototypical manifold for liquid metal blankets, Nucl. Fusion 63 (8) (2023) 086005, http://dx.doi.org/10.1088/1741-4326/acdc14.

[34] N. Razuvanov, N. Pyatnitskaya, P. Frick, I. Belyaev, V. Sviridov, Experimental study of liquid metal heat transfer in a vertical duct affected by coplanar magnetic field: Upward flow, Int. J. Heat Mass Transfer 156 (2020) 119746, http://dx.doi.org/10.1016/j.ijheatmasstransfer.2020.119746.

[35] C. Wong, J.-F. Salavy, Y. Kim, I. Kirillov, E.R. Kumar, N. Morley, S. Tanaka, Y. Wu, Overview of liquid metal TBM concepts and programs, Fusion Eng. Des. 83 (7–9) (2008) 850–857, http://dx.doi.org/10.1016/j.fusengdes.2008.06.040.

[36] S. Malang, R. Mattas, Comparison of lithium and the eutectic lead-lithium alloy, two candidate liquid metal breeder materials for self-cooled blankets, Fusion Eng. Des. 27 (1995) 399–406, http://dx.doi.org/10.1016/0920-3796(95)90151-5.

[37] D. Martelli, A. Venturini, M. Utili, Literature review of lead-lithium thermophysical properties, Fusion Eng. Des. 138 (2019) 183–195, http://dx.doi.org/10.1016/j.fusengdes.2018.11.028.

[38] F. Nicoud, F. Ducros, Subgrid-scale stress modelling based on the square of the velocity gradient tensor, Flow Turbul. Combust. 62 (3) (1999) 183–200, http://dx.doi.org/10.1023/a:1009995426001.

[39] F. Fico, I. Langella, H. Xia, Large-eddy simulation of magnetohydrodynamics and heat transfer in annular pipe liquid metal flow, Phys. Fluids 35 (5) (2023) http://dx.doi.org/10.1063/5.0143687.

[40] S. Patankar, C. Liu, E. Sparrow, The periodic thermally developed regime in ducts with streamwise periodic wall temperature or heat flux, Int. J. Heat Mass Transfer 21 (5) (1978) 557–566, http://dx.doi.org/10.1016/0017-9310(78)90052-2.

[41] G. Ahlers, E. Brown, F.F. Araujo, D. Funfschilling, S. Grossmann, D. Lohse, Non-Oberbeck–Boussinesq effects in strongly turbulent Rayleigh–Bénard convection, J. Fluid Mech. 569 (2006) 409, http://dx.doi.org/10.1017/s0022112006002916.

[42] H.G. Weller, G. Tabor, H. Jasak, C. Fureby, A tensorial approach to computational continuum mechanics using object-oriented techniques, Comput. Phys. 12 (6) (1998) 620, http://dx.doi.org/10.1063/1.168744.

[43] M.-J. Ni, R. Munipalli, P. Huang, N.B. Morley, M.A. Abdou, A current density conservative scheme for incompressible MHD flows at a low magnetic Reynolds number, part I: On a rectangular collocated grid system, J. Comput. Phys. 227 (1) (2007) 205–228, http://dx.doi.org/10.1016/j.jcp.2007.07.023.

[44] J.C.R. Hunt, Magnetohydrodynamic flow in rectangular ducts, J. Fluid Mech. 21 (4) (1965) 577–590, http://dx.doi.org/10.1017/s0022112065000344.

[45] S. Gavrilakis, Numerical simulation of low-Reynolds-number turbulent flow through a straight square duct, J. Fluid Mech. 244 (-1) (1992) 101, http://dx.doi.org/10.1017/s0022112092002982.

[46] F.B. Gessner, The origin of secondary flow in turbulent flow along a corner, J. Fluid Mech. 58 (01) (1973) 1, http://dx.doi.org/10.1017/s0022112073002090.

[47] A. Sekimoto, G. Kawahara, K. Sekiyama, M. Uhlmann, A. Pinelli, Turbulence- and buoyancy-driven secondary flow in a horizontal square duct heated from below, Phys. Fluids 23 (7) (2011) 075103, http://dx.doi.org/10.1063/1.3593462.